Synthesis and characterization of rare-earth orthoferrite LnFeO3 nanoparticles bioimaging

Sonia Pinho, João Amaral, Alain Wattiaux, Mathieu Duttine, Marie-Hélène Delville, Carlos F. G. C. Geraldes

Synthesis and characterization of rare earth orthoferrite $LnFeO_3$ nanoparticles for bioimaging

Sonia L.C. Pinho,[a, b, c] João S. Amaral,[d] Alain Wattiaux,[b] Mathieu Duttine,[b] Marie-Hélène Delville,[b]* and Carlos F.G.C. Geraldes[e,f]*

Dedication ((optional))

Abstract: A combination of sol–gel synthesis and thermal decomposition was developed for preparing nano-sized, perovskite-type $LnFeO_3$ (Ln = Eu, Gd, Tb) powders. Perovskite-type powders with crystalline particles of 100 nm average size, as determined by transmission electron microscopy (TEM), could be obtained after a thermal treatment at 800 °C. The perovskite nanoparticles (NPs) were further characterized by X-ray powder diffraction and Mössbauer spectroscopy. These were in agreement with the pure perovskite $LnFeO_3$ structure with the expected Zeeman sextet corresponding to a magnetically ordered phase. Magnetization measurements (M(H)) at 5 K and 300 K showed a behavior that is dominated by antiferromagnetic interactions and weak ferromagnetism in $EuFeO_3$, while for Ln = Gd,Tb they were dominated by the low ordering temperature Ln magnetic sublattice. The colloidal aqueous NPs suspensions exhibited no significant leaching of free Ln^{3+} ions. Their relaxivities define them as potential T_2 MRI contrast agents for further biomedical applications. The NPs showed fast uptake and no cytotoxicity at concentrations below 62.5 µg/mL with respect to Hela cells.

Introduction

Magnetic resonance imaging (MRI) has emerged as one of the most powerful clinical imaging tools due to its superb spatial resolution and excellent soft tissue contrast, which mostly results from intrinsic differences in the relaxation times ($T_{1,2}$) of tissue water protons. The contrast between normal and diseased tissues can be dramatically improved by the use of contrast agents (CAs), namely paramagnetic Gd^{3+}-based chelates, e.g. Gd-DTPA or superparamagnetic iron-oxide based nanoparticles (T_1- and T_2-shortening agents, respectively).[1-3] There is a strong interest in developing novel nanoparticle based CAs with enhanced T_1 and/or T_2 relaxation properties.[4-9] It was recently shown that gadolinium oxide (Gd_2O_3) nanoparticles (NPs) can act as T_1 CAs, enhancing MRI signal intensity, due to the availability of Gd^{3+} ions at their surface to interact with water,[10, 11] in particular for very small (5-10 nm) nanocrystals.[12-14]

NPs with multimodal contrast imaging capabilities can offer synergistic advantages over those active for only a single modality.[15-18] Several T_1-T_2 bimodal CAs for MRI have been developed,[19] mostly integrating a superparamagnetic iron oxide (magnetite or maghemite) core in a Gd^{3+}-containing paramagnetic shell.[20-22] However, in this arrangement, the strong magnetic field from the superparamagnetic core opposes the magnetic field created by the paramagnetic shell, decreasing its T_1 relaxation effect.[22] If the paramagnetic material is located inside the superparamagnetic iron oxide, their magnetic fields reinforce each other, enhancing the T_1 contrast. Such a synergistic T_1-T_2 relaxation effect has been reported using Gd_2O_3 ultra-small clusters embedded in iron oxide nanoparticles.[23]

An alternative to generate T_1-T_2 relaxation effects is to use rare-earth orthoferrite NPs. High-quality nanocrystalline rare-earth orthoferrites $LnFeO_3$ (Ln = rare earth) with a perovskite structure have been thoroughly studied since the 1960s because of their unique physical and chemical properties for various applications such as catalysts,[24, 25] gas separators,[26] sensors[27] and opto-magnetic materials.[28-35] The synthesis of the specific $LnFeO_3$ phases is very challenging, since undesired phases can co-exist. An example is the garnet phase ($Ln_3Fe_5O_{12}$) with a thermodynamically more stable phase when compared to $LnFeO_3$.[32] As the ionic radius of the Ln^{3+} decreases, the tolerance factor, t, defined by Goldschmidt,[31, 36] becomes smaller than the ideal value in the 0.9-1.0 range. This indicates that the perovskite structure distortion increases and becomes less stable due the increasing Fe^{3+} to Ln^{3+} ionic radius quotient, as the Ln^{3+} ions become too small to fit ideally into their eight coordination interstitial sites provided by the O^{2-} ions.[37, 38] Therefore, the synthesis of $LnFeO_3$ perovskites becomes progressively more difficult with decreasing the ionic radius of the Ln element.[39, 40] The preparation of $LnFeO_3$ has been achieved by many methods, including sol-gel,[41-44] sonochemical,[31] microwave-assisted,[45] combustion synthesis,[30, 46-50] hetero-bimetallic precursor methods,[32] and solvothermal [51] and hydrothermal synthesis.[52]

[a] Dr S. L.C. Pinho,
Department of Chemistry, CICECO, University of Aveiro,
3810-193 Aveiro, Portugal
[b] Drs S. L.C. Pinho, A. Wattiaux, M. Duttine, M.-H. Delville
CNRS, Univ. Bordeaux, ICMCB, UMR 5026
F-33600 Pessac, France
E-mail: marie-helene.delville@icmcb.cnrs.fr
[c] Dr S. L.C. Pinho
present address: Biocant – Biotechnology Innovation Center,
Parque Tecnológico de Cantanhede, Núcleo 4, Lote 8,
3060-197 Cantanhede, Portugal
[d] Dr João S. Amaral
Department of Physics, CICECO,
University of Aveiro, 3810-193 Aveiro, Portugal
[e] Pr.Carlos F.G.C. Geraldes
Department of Life Sciences, Faculty of Science and Technology,
Calçada Martim de Freitas, University of Coimbra,
3000-393 Coimbra, Portugal
E-mail: geraldes@ci.uc.pt
[f] Pr.Carlos F.G.C. Geraldes
Coimbra Chemistry Center, Rua Larga, University of Coimbra, 3004-535 Coimbra, Portugal

Supporting information for this article is given via a link at the end of the document

In this work, we report a sol-gel / auto-combustion method / approach to prepare monophasic nanosized $LnFeO_3$ (Ln = Eu, Tb and Gd) powders. The nanomaterials were characterized by transmission electron microscopy (TEM), X-ray powder diffraction (XRD), magnetization measurements and Mössbauer spectroscopy. The stability of aqueous suspensions of the $LnFeO_3$ nanoparticles (NPs) was also studied by zeta potential and Ln^{3+} leaching measurements. The water proton relaxation effects of the $LnFeO_3$ nanoparticles were also studied, in order to assess their utility as CAs for MRI. Finally, the cell internalization and cytotoxicity of the nanoparticles in Hela cells was investigated.

Results and Discussion

Synthesis and Characterization of the Nanoparticles

Aqueous suspensions of $LnFeO_3$ NPs were synthesized by sol-gel/auto-combustion, as described in the experimental section. The TEM images for $LnFeO_3$ reveal spherical, particles with an average size D_{TEM} of 100 ± 30 nm (Table 1), as illustrated in the case of $GdFeO_3$ in Figure 1.

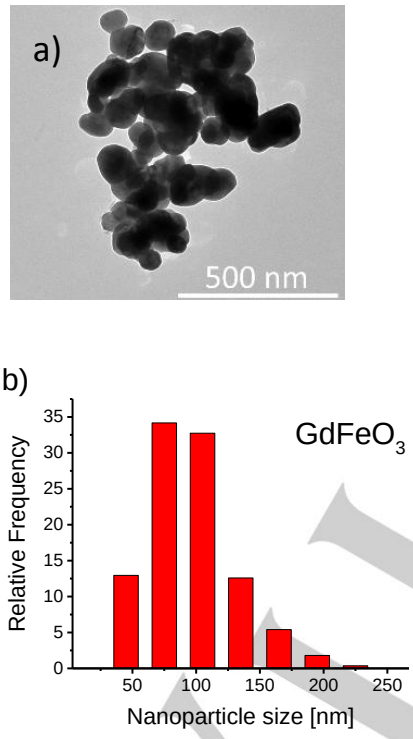

Figure 1. a) TEM image of the $GdFeO_3$ NPs; b) histogram depicting the $GdFeO_3$NPs size distribution. Size distributions for $EuFeO_3$ and $TbFeO_3$ are given in SI (Figure S1).

The elemental analyses of the different $LnFeO_3$ NPs (Table 1) show that the Ln/Fe concentration ratios are very close but not equal to 1.0, as expected, significant of the presence of a small amount of a second phase which was however difficult to identify due to its lack of crystallinity as shown later on.

Table 1. Elemental composition of samples $LnFeO_3$ (Ln = Eu, Gd and Tb) ascertained by ICP-OES and NPs size by TEM (nm)

Ln	[Ln]/[Fe]	TEM (nm)
Eu	0.98 (1)	107 ± 30
Gd	0.98 (1)	96 ± 31
Tb	0.92 (1)	115 ± 31

Figures 2 to 4 show the X-ray diffraction profiles for the different compounds, which exhibit the typical Bragg reflections of the rare earth orthoferrites, indicating that the nanomaterials present a perovskite structure (space group *Pbnm*) and are crystalline.[37, 38] The peak present at ~27º in the diffraction data of $EuFeO_3$ comes from the graphite sample holder. The diffractograms were fitted using the Le Bail method, considering a single phase of orthoferrite with a perovskite structure and the red line represents the model obtained with this refinement; the dashed green line being the difference between the experimental data and the fit.

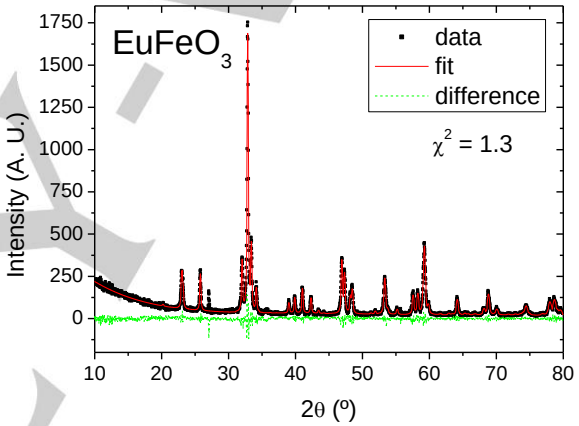

Figure 2. (Color online) X-Ray diffraction data of $EuFeO_3$ (solid points), best fit (red line) and data to fit difference (dashed green line).

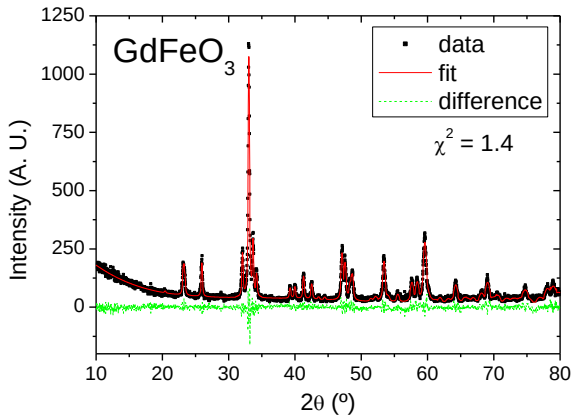

Figure 3. ((Color online) X-Ray diffraction data of $GdFeO_3$ (solid points), best fit (red line) and data to fit difference (dashed green line). JCPDS 47-0067

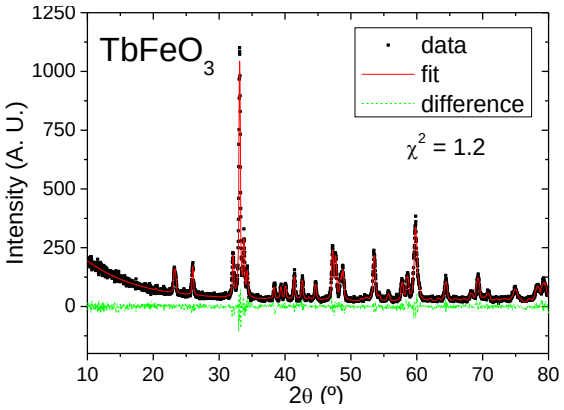

Figure 4. (Color online) X-Ray diffraction data of $TbFeO_3$ (solid points), best fit (red line) and data to fit difference (dashed green line).

Table 2 shows the resulting lattice parameters and goodness of fit values for the studied $LnFeO_3$ samples. They are in good agreement with those reported in bulk samples[53] and recent work on micrometer-sized rare-earth orthoferrite particles[54] or NPs.[43] The $LnFeO_3$ structure has a considerably distorted perovskite geometry, because Ln^{3+} (Gd^{3+}, Eu^{3+}, or Tb^{3+}) has a coordination number of 8, whereas the A-site in the ideal perovskite has a coordination number of 12. This is due to the less favorable Fe^{3+} to Ln^{3+} ionic radius quotient with r (Fe^{3+})/r (Eu^{3+}) ≈ 0.605, r (Fe^{3+})/r (Gd^{3+}) ≈ 0.612 and r (Fe^{3+})/r (Tb^{3+}) ≈ 0.620,[55] as opposed to the 0.56 value for a typical cubic perovskite such as in $SrTiO_3$. In none of these diffraction patterns, we were able to identify any of the usually encountered phases beside $LnFeO_3$.

Table 2. Lattice parameters and of the studied $LnFeO_3$ samples.

Compound	a (nm)	b (nm)	c (nm)	V (nm^3)	χ^2
$EuFeO_3$	0.5369	0.5593	0.7683	0.2307	1.3
$GdFeO_3$	0.5350	0.5607	0.7669	0.2301	1.4
$TbFeO_3$	0.5328	0.5593	0.7645	0.2278	1.2

Mössbauer spectroscopy

Mössbauer room temperature experimental spectra of $LnFeO_3$ tare illustrated in Figure 5 with their calculated spectra, while the hyperfine parameters are gathered in Table 3. For the three compounds, the major contribution is described by the presence of a magnetically ordered sextet.[56-67] The refined values of the hyperfine parameters are consistent with high-spin iron(III) ions located at a crystallographic site in octahedral symmetry (site 1) in good agreement with the perovskite structure of these compounds. The isomer shift (δ) values determined for the $EuFeO_3$ and $TbFeO_3$ samples are very close to those reported in previous studies for similar compounds.[56, 57, 61, 66-68]The values of the hyperfine field are around 50 T, indicating that the hyperfine field is very close to the saturated field. These results are in good agreement with the XRD crystallographic studies. $GdFeO_3$ is the only one to be pure within the limit of detection of the technique while the two other compounds, $EuFeO_3$ and $TbFeO_3$, both exhibit an additional signal, which is not magnetically ordered at room temperature. This minor component (about 3% in relative area), described by a quadrupole doublet with an isomer shift $\delta \approx 0.15$-0.20 mm/s and a quadrupole splitting $\Delta \approx 0.4$-0.5 mm/s, was not detected on the respective XRD patterns. It could be associated with an unidentified iron-containing impurity as suggested by the results of ICP elemental analyses.

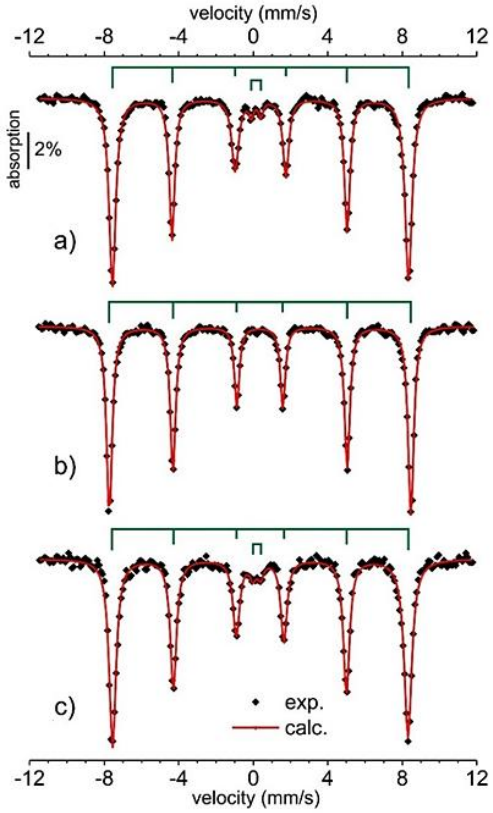

Figure 5. ^{57}Fe room temperature Mössbauer spectra of (a) $EuFeO_3$, (b) $GdFeO_3$ and (c) $TbFeO_3$. The refined hyperfine parameters associated with the magnetic sextets and paramagnetic quadrupole doublets are reported in Table 3.

Table 3. Refined hyperfine parameters estimated from the analysis of the ^{57}Fe Mössbauer spectra presented in Figure 5. δ: isomer shift (relative to α-Fe) at room temperature, Δ: quadrupole splitting, ε: quadrupole shift, H: hyperfine magnetic field, Γ: Lorentzian linewidth.

Compound	δ (mm/s)	Δ (mm/s)	2ε (mm/s)	H (T)	Γ (mm/s)	area (%)
$EuFeO_3$						
sextet	0.376(4)	-	0.046(5)	50.1(5)	0.44(5)	97(1)
doublet	0.15(2)	0.51(2)	-	-	0.27(3)	3(1)
$GdFeO_3$						
sextet	0.363(4)	-	0.002(5)	50.0(5)	0.34(3)	100
$TbFeO_3$						
sextet	0.370(4)	-	0.021(5)	49.5(5)	0.44(5)	97(1)
doublet	0.19(2)	0.37(2)	-	-	0.37(3)	3(1)

Moreover, the high values of the Lorentzian linewidth (Γ) may reflect some local disorders in the iron environment (cationic heterogeneous distribution, site distortion) that could be related to the particle size and size dispersity (see Figure 1 and Table 1).

Magnetization studies

The magnetization of the $LnFeO_3$ NPs was studied as a function of the applied magnetic field. Their magnetic behavior results

from the contribution of two magnetic sub-lattices: an antiferromagnetic iron oxide lattice with the spins coupled via a Fe^{3+}- O^{2-}- Fe^{3+} super exchange mechanism, and a paramagnetic contribution from non-coupled Ln^{3+} ions. Figure 6A shows the magnetization dependence of the $EuFeO_3$ sample on applied magnetic field, at 5 K. In accordance with reports of small spin canting phenomena in the Fe-containing sub-lattice, resulting from the distorted perovskite structures, which induce weak ferromagnetism in this system,[31, 69, 70] we observe a small hysteresis with a coercive field of about 330 Oe, together with typical mainly antiferromagnetic behavior of the Fe sub-lattice.

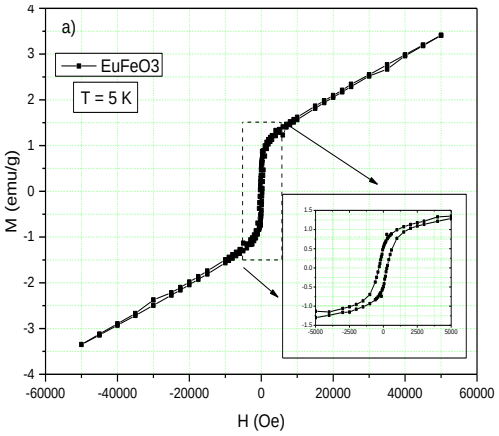

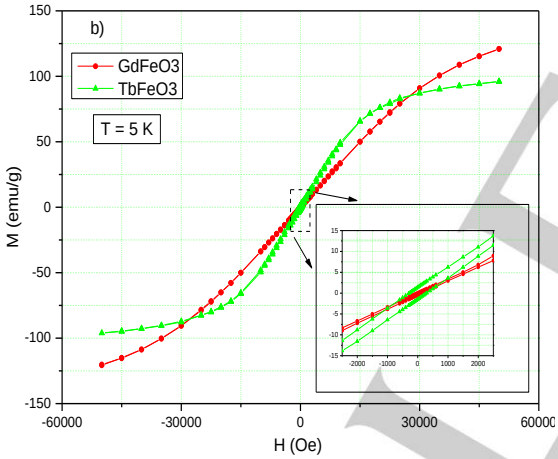

Figure 6. Magnetization versus applied magnetic field at 5 K a) for the $EuFeO_3$ sample; b) for the $LnFeO_3$ (Ln = Gd, Tb) samples. Inset shows detail at low field.

Figure 6b shows the magnetization versus field dependence at 5 K for the $GdFeO_3$ and $TbFeO_3$ samples. The much higher values of magnetization (M_S) as compared to the $EuFeO_3$ sample show that the magnetization versus applied field behavior at this temperature is dominated by the rare-earth ions. In the case of $TbFeO_3$, the rare-earth sub-lattice is magnetically ordered below 8.4 K, justifying the observed approach to saturation at 5 K.[71-73] Comparatively, the ordering temperature for the Gd sub-lattice in $GdFeO_3$ is 2.5 K,[74] and the behavior is paramagnetic. The magnetization curve for $GdFeO_3$ at 5 K is significantly different from that reported for much smaller (3.5-5.0 nm) $GdFeO_3$ NPs at 2K, with a saturation magnetization M_S = 80 emu.g^{-1}.[43]

At 300 K, for all the $LnFeO_3$ systems studied, there is no sign of saturation even at 50 KOe (5 T). In the case of $EuFeO_3$, where the magnetization comes only from the Fe sub-lattice, a maximum value of ~2.5 emu/g is observed, as shown in Figure 7. For $GdFeO_3$ and $TbFeO_3$, these values are ~6 emu/g and ~9 emu/g respectively. Assuming that in these two compounds the magnetic contribution of the Fe sublattice is similar to that observed in $EuFeO_3$ at this temperature and applied field range, the magnetic Gd/Tb ion contribution to the total magnetization is comparable to that of the Fe sub-lattice.

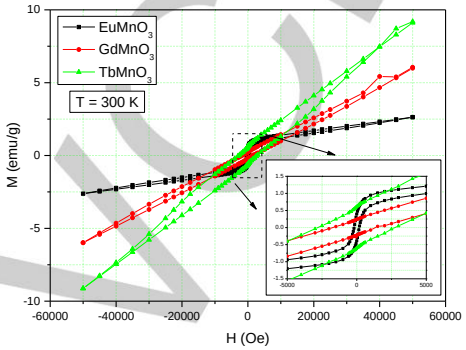

Figure 7. Magnetization versus applied magnetic field for the $LnFeO_3$ (Ln = Eu, Gd, Tb) samples, at 300 K. Inset shows detail at low field.

There is nonetheless a magnetic interaction between the rare-earth ions and the Fe lattice, as the coercive field and hysteresis width noticeably increase with the presence of a magnetic rare-earth ion. The magnetization values at 300 K reported here are in agreement with previous reports on the properties of these rare-earth orthoferrite materials [50, 75-77] while coercive field values in the range of the hundreds of Oe are comparable to recent reports.[31, 32]

Solution studies

The zeta potential titration as a function of pH confirmed the negative charge of the NPs over most of the pH range (Supplementary Information, Figure S2), with a point of zero charge close to 3 providing a colloidal stability in physiological conditions.

Due to the magnetic properties of the $LnFeO_3$ NPs, they were tested as T_1-T_2 MRI CAs. Table 4 shows the water ^{1}H relaxivity values (r_1 and r_2) and the r_2/r_1 ratios, measured at 20 MHz and 298 K and 310 K, for clear suspensions of the $EuFeO_3$, $TbFeO_3$, and $GdFeO_3$ NPs in water and compares them with literature data.[43] The relaxivities were obtained from the observed linear dependence of the R_i ($R_i = 1/T_i$, i = 1, 2) relaxation rates on the concentration of the Ln^{3+} ions in the samples, using at least five independent measurements at concentrations between 0 and 2 mM, as shown in SI Figures S3 and S4.

The observed r_1 values are quite low for all the studied samples, although slightly larger for Ln = Gd and Tb than for Eu. The r_1 and r_2 relaxivities can have contributions from inner-sphere (IS) and outer-sphere (OS) mechanisms.[1, 5, 78] The IS mechanism results from the water molecules directly coordinated to the Ln^{3+} ions on the surface of the NPs, which affects their proton relaxation through contact and dipolar terms (for Gd^{3+}) and also a Curie term (for the other paramagnetic Ln^{3+}). It depends on the

longitudinal relaxivity of the inner-sphere water molecules directly coordinated to the surface Ln^{3+} ions, their hydration number, and the surface-to-volume (S/V) ratio of the NPs.[78, 79] The OS mechanism results from the diffusion of the water molecules in the magnetic field inhomogeneities created by the magnetized NPs in their vicinity, and does not contain the contact term. It depends on their distance of closest approach to the NPs surface, as well as on the NPs size and magnetization.[5, 78] The very small r_1 values observed for the $LnFeO_3$ NPs of 100 nm size (Table 4) are similar to those reported at low magnetic fields (0.47-1.5 T) for Dy_2O_3[79, 80] and Gd_2O_3 [81-83] NPs of similar size (20-100 nm). There are however significant differences relatively to the r_1 data reported for analogous $GdFeO_3$ nanomaterials (Table 4),[43] which have larger r_1 values. This is attributed to the much smaller crystal size (3.5-5.0 nm) of these two samples. It is well-known that the r_1 values for NPs increase as their size decreases, as the number of paramagnetic metal ions at the surface increases with their (S/V) ratio. Depending on the magnetic field, the r_1 values of Gd_2O_3 NPs can go up to 12 (1.5 T) or 10 $s^{-1}mM^{-1}$ (3 T) with optimal particle sizes of 1.6 and 3.8 nm, respectively.[12, 14, 79, 83-86]

The r_2 values observed for the $LnFeO_3$ NPs (Table 4) are considerably higher than r_1, giving r_2/r_1 values much larger than 2, which corresponds to a dominant T_2-weighted (negative-contrast) mechanism. The relative r_2 values at 298 K increase in the order Gd < Eu < Tb, which partially disagrees with the relative magnetization values (Gd < Tb < Eu, Figure 7) observed at 0.47 T (4700 Oe), where, due to the observed hysteresis, the upfield M(H) traces were considered. The r_2 value observed for $EuFeO_3$, where the magnetization comes only from the Fe sub-lattice, are smaller than would be expected from the OS mechanism.[78] The r_2 values previously reported for the much smaller $GdFeO_3$ NPs at 1.5 T are somewhat larger (Table 4)[43] as a result of the higher magnetic field (1.5 T) used in that study. These results can be compared with reported r_2 data for paramagnetic Ln_2O_3 NPs in different experimental conditions. At the same magnetic field, the r_2 values of the paramagnetic Ln_2O_3 NPs of the same size have been found to increase with their magnetization, which is proportional to the square of the effective magnetic moment (μ_{eff}) of the Ln^{3+} ion (in the order Eu < Gd < Tb).[78, 81] For the same Ln, r_2 was found to increase with the magnetic field B_0 or with B_0^2. [12, 78, 80, 81] The dependence of r_2 on the particle size is more complex, as found experimentally [12, 14, 78-87] and predicted by the OS theory.[78, 88-90] For small particles, the Motional Averaging Regime (MAR) operates, and r_2 is proportional to $(\mu_{eff})^2B_0^2$ and inversely proportional to the radius of the NP. For large particles, the Static Diffusion Regime (SDR) predicts that r_2 is proportional to $(\mu_{eff})^2B_0$ and that it becomes dependent on the time interval between two consecutive 180° pulses (τ_{CP}) in the Carr–Purcell–Meiboom–Gill (CPMG) pulse sequence used to determine the T_2 values. This dependence is also influenced by the particle coating, as it may influence the distance of closest approach of the water molecules to the NPs surface.

Table 4. ^{1}H relaxivities, r_{ip} (i = 1,2), determined at 20 MHz (0.47 T), at 298 K and 310 K, for aqueous suspensions of $EuFeO_3$, $TbFeO_3$, and $GdFeO_3$, compared with values from the literature.

Compound size (nm)	r_1 ($s^{-1}mM^{-1}$)		r_2 ($s^{-1}mM^{-1}$)		r_2/r_1		Ref.
	298 K	310 K	298 K	310 K	298 K	310 K	
$EuFeO_3$ 107 ± 30	0.20 ± 0.01	0.20± 0.01	6.18 ± 0.06	6.45 ± 0.01	30.9	32.3	This work[a]
$TbFeO_3$ 96 ± 31	0.68 ± 0.05	0.41± 0.05	9.45 ± 0.02	9.38 ± 0.01	13.90	22.9	This work[a]
$GdFeO_3$ 115 ± 31	0.60 ± 0.02	0.59± 0.07	5.65 ± 0.02	3.84 ± 0.01	9.42	6.52	This work[a]
$GdFeO_3$ dialysed 4h 3.5	4.5		11.3		2.5		[43] [b]
$GdFeO_3$ dialysed 120h 5	11.9		15.2		1.3		[43] [b]
Gd-DTPA	4.1		4.7		1.1		[14] [c]

[a] Measured at 0.47 T (20 MHz); [b] Measured at 1.5 T (64 MHz); [c] Measured at 1.5 T (64 MHz)

Regarding the leaching of Ln^{3+} ions from the NPs, when we compare the concentration of free Ln^{3+} ions and the initial Ln within the NPs, no significant leaching of Ln^{3+} ions was observed in aqueous dispersions of the NPs stored at 4 $_o$C for a week (0.42% for Eu^{3+}, 0.87% for Tb^{3+} and 1.4 % for Gd^{3+}, see Figure S5), as determined quantitatively using a spectrophotometric xylenol orange method.[91] Values below 1.5 % were obtained regarding leaching of Ln^{3+} ions form the NPs. This is an important condition to minimize their *in vitro* and *in vivo* toxicity.

Cell internalization and cytotoxicity of NPs

A preliminary assessment of the biological effect of the NPs on cell metabolism was evaluated after exposing Hela cells (7 x 10^3 cell/well) to increasing concentrations of NPs (from 7 to 250 µg/mL) for 24 h. The uptake of NPs can cause changes in cell morphology, which can be observed after only a few hours of exposure to the NPs, suggesting interference with normal cell function. Reduction of ATP levels is considered a reliable cell viability marker.[92] Cell metabolism was assessed by ATP production using a CellTiter-Glo ® Cell Viability Assay. Figure 8 shows a decrease in ATP content of cells exposed for 24 h to higher concentrations of NPs. NPs concentrations equal or higher than 62.5 µg/mL showed extremely significant impaired ATP production relative to control ($P < 0.0001$ or $P < 0.01$). Similar findings have been reported in a previous study for different sized Fe_2O_3 NPs.[93] For concentrations below 62.5 µg/mL, the ATP production showed non-significant changes with respect to the controls for the three types of NPs, indicating no cytotoxicity of these NPs at concentrations below 62.5 µg/mL with respect to Hela cells. Further tests should be performed to assess in more detail the cytotoxicity of these particles in other cell lines. Nevertheless, the full viability of cells was ensured for the experimental concentration of 50 µg/mL used throughout our studies.

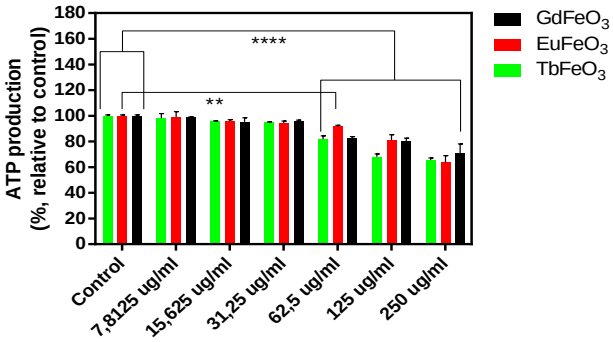

Figure 8. Effect of increasing concentrations of NPs ($EuFeO_3$, $TbFeO_3$ and $GdFeO_3$) upon ATP production by Hela cells. Cells were incubated with the NPs for 4 h, washed and left for 20 h. The results are expressed as mean ± SD (n = 3). ** and **** denote statistical significance (P < 0.01 and P < 0.0001, respectively)

The three systems ($EuFeO_3$, $TbFeO_3$ and $GdFeO_3$) were studied regarding their cell internalization and cytotoxicity. The internalization kinetics of the NPs in Hela cells was studied for three different incubation times: 2, 4 and 6 h and 50 µg/mL of NPs. To quantify the real amounts of NPs internalized in Hela cells at different times, inductively coupled plasma mass spectrometry (ICP-MS) was used (Figure 9). The results indicate a time-dependent increase in the uptake of the NPs by the cells. The internalization kinetics of the three types of NPs is quite similar, where a plateau (~2.0 x 10^5 NPs per cell), after 4 h, is reached for the three systems and presents the same internalization efficiency with no statistical significance. Nevertheless, statistical difference between, the $GdFeO_3$ and the $EuFeO_3$ system, as for two different time points (4h and 6h) the $EuFeO_3$ system showed less uptake.

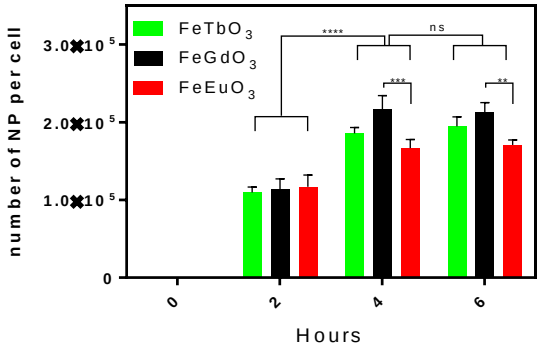

Figure 9. Quantification of NPs per Hela cells determined by ICP-MS analysis. Cells were incubated with NPs ($EuFeO_3$, $TbFeO_3$ and $GdFeO_3$) for 2 h, 4 h and 6 h. After the incubation, the cells were washed, trypsinized and finally freeze-dried. The number of NPs was determined by average NPs size and crystal unit method. The results are expressed as mean ± SD (n = 3). **, *** and **** denote statistical significance (P < 0.01, P < 0.001, and P < 0.0001, respectively).

Conclusions

It has been demonstrated that reproducible crystalline powders made of spherical, nanosized (100 ± 30 nm average diameter), perovskite-type $LnFeO_3$ (Ln = Eu, Gd, Tb) particles can be synthesized by sol–gel auto-combustion after a thermal treatment at 800 °C. Characterization by X-ray powder diffraction and Mössbauer spectroscopy confirmed a pure perovskite $LnFeO_3$ structure for $GdFeO_3$ whereas an additional 3% intensity quadrupole doublet was detected by Mössbauer in the case of $EuFeO_3$ and $TbFeO_3$. The field-dependent magnetization measurements at 5 K and 300 K revealed behaviour dominated by antiferromagnetic interactions and weak ferromagnetism of the Fe sub-lattice in the case of $EuFeO_3$, while for Ln = Gd, Tb it becomes dominated by the contribution of the low ordering temperature Ln magnetic sub-lattice. The negatively charged colloidal aqueous NPs suspensions were stable and showed no significant leaching of free Ln^{3+} ions. These NPs exhibit very small r_1 relaxivities and larger r_2 values, which are proportional to their magnetization at 0.47 T (4.7 KOe). The NPs showed a fast uptake and no cytotoxicity at concentrations below 62.5 µg/mL with respect to Hela cells. These characteristics define them as potentially useful T_2-weighed (negative contrast) MRI contrast agents for further biomedical applications.

Experimental Section

Materials and purification methods: Fe $(NO_3)_3$•$9H_2O$ (>98%), $Gd(NO_3)_3$•$6H_2O$ (99.99%), $Eu(NO_3)_3$•$5H_2O$ (99.9%), $Tb(NO_3)_3$•$5H_2O$ (99.9%) and nitric acid were purchased from Sigma-Aldrich and used as received. Water was deionized (resistivity larger than 18 MQ). All the other reagents, of analytical grade, were purchased from Sigma-Aldrich and used without further purification.

Preparation of the nanoparticles: According to the stoichiometric composition reactants, specified amounts of Fe $(NO_3)_3$•$9H_2O$ and hydrated $Ln(NO_3)_3$ (Ln = Eu, Gd, Tb) were first dissolved in nitric acid solution as follows: 1 mmol of of Fe $(NO_3)_3$•$9H_2O$, 1 mmol of $Eu(NO_3)_3$ and 1 mmol HNO_3. 3 mmol of citric acid were also dissolved into the nitric solution. The sol was heated in a sand bath at 200ºC in order to evaporate all the solvent and a brown, puffy, porous dry gel was formed. Auto-combustion of the formed gel was induced with a flame until the gel burned completely into a loose powder, known as as-synthesized powder. The calcination took place according to the following cycle: 1.5 h increasing sample temperature to 400 ºC, 2 h at 400 ºC, milling the sample, 1.5 h temperature increase to 800 ºC, mill the sample, and calcine it for 6h at 800 ºC.

Particle Characterization: The morphologies of the nanoparticles were observed by TEM measurements performed at room temperature on a JEOL JEM-2000 FX transmission electron microscope using an accelerating voltage of 200 kV. Drops of diluted water dispersions of nanoparticles were air-dried on amorphous carbon films deposited on 200-mesh copper grids. Average particle sizes (D_{TEM}) were calculated by analyzing at least 250 particles randomly selected from TEM micrographs. The iron, europium, terbium, and gadolinium contents were measured by inductively coupled plasma / optical emission spectrometry ICP/OES (ES720, Varian) equipped with a crossflow nebulizer. Solutions for each element with a concentration of 1 g/L were used to prepare the standard solutions (SCP Science to Paris) and were used as internal standard to evaluate the instrumental drift.

Diffraction data were obtained on a Philips X'Pert MPD PRO powder diffractometer in the Bragg– Brentano geometry, using Cu-K_α radiation ($K_{\alpha1}$= 1.54059 Å and $K_{\alpha2}$= 1.54441 Å, 45 kV, 40 mA). The data collections were made in the 6–80 º 2θ range with a 0.02º step. Samples are shown to be single-phase, with peaks indexed to the D_{2h}^{16} – Pbnm space group (62). The diffraction data were analyzed using the Le Bail whole pattern fitting method, as implemented in the PowderCell software.

The magnetization of dried nanoparticles was measured using a Quantum Design MPMS-5S SQUID magnetometer. Magnetization values were acquired as a function of applied magnetic field [$M(H)$] by using about 10 mg of nanopowder per measurement. Hysteresis cycles were measured at 5 K and 300 K at a magnetic field range of -50000 Oe to 50000 Oe.

^{57}Fe Mössbauer spectra were recorded at 293 K in a conventional transmission geometry spectrometer using a triangular driving, with a 30 mCi ^{57}Co (Rh matrix) source. The spectra were analysed by using the least squares method assuming Lorentzian line shapes. The isomer shifts values are relative to α-Fe at 293 K. Powder samples were measured in acrylic holders of 1.5 mm diameter, covering all the surface area. When necessary, the samples were mixed with boron nitride to be able to cover the whole surface.

The zeta potential of the nanoparticles in solution was assessed using a Zetasizer 3000HSA setup (Malvern Instruments) equipped with a He-Ne laser (50 mW, 532 nm). The zeta potential measurement based on laser Doppler interferometry was used to measure the electrophoretic mobility of the nanoparticles. Measurements were performed for 20 s using a standard capillary electrophoresis cell. The dielectric constant was set to 80.4 and the Smoluchowsky constant was 1.5.

^{1}H longitudinal and transverse relaxation times (T_1 and T_2 respectively) of aqueous suspensions of nanoparticles were measured by magnetic resonance relaxometry (Bruker Minispec mq20 relaxometer operating at a magnetic field of 0.47 T, corresponding to a proton Larmor frequency of 20 MHz). T_1 values were measured using the inversion recovery pulse sequence, while T_2 values were measured using a Carr-Purcell-Meiboom-Gill (CPMG) pulse sequence. A linear dependence between the inverse proton relaxation times (*i.e.* the water proton relaxation rates $R_i = 1/T_i$, i = 1, 2) and the Ln^{3+} concentration is expected for the magnetic nanomaterials, in accordance with the equation $(1/T_{i,obs}) = (1/T_{i,0}) + r_i$ [Ln], where $T_{i,obs}$ (i = 1,2) is the relaxation time measured experimentally in the presence of the magnetic nanomaterial, $T_{i,0}$ is the relaxation time of pure water in the absence of the contrast agent, [M] is the Ln^{3+} concentration (mM) in the contrast agent and r_i is the longitudinal (i = 1) or transverse (i = 2) relaxivity (*i.e.* proton relaxation rate enhancement *per* mM Ln^{3+}). All the experimental values were corrected for the diamagnetic aqueous contributions under the same conditions.

The quantification of the free Ln^{3+} (Ln = Eu, Gd, Tb) ions leached from the NPs was carried out using the spectrophotometric method based on the differences in the visible spectra of free and complexed xylenol orange dye, as described in the literature.[91] Briefly, 3.43 g of xylenol orange were dissolved in 250 mL buffer solution (acetic acid and NaOH, pH = 5.81) and the solution was stored at 4 ºC for one week. An aqueous dispersion of the $LnFeO_3$ NPs ($EuFeO_3$: 0.77 mM, $GdFeO_3$: 1.35 mM and $EuFeO_3$: 1.32 mM) in the buffer xylenol orange solution was also stored at 4º C for a week. Calibration curves were built with free Gd^{3+} ions in solutions (0–70 µM), prepared with the buffer solution and dissolving $LnFeO_3$ with nitric acid (HNO_3). The calibration curve was determined from the plot of the ratio between the integrated intensities of the UV-visible absorption bands at 563 and 446 nm *vs.* the Ln^{3+} concentration (Fig S5A). Finally, the absorption spectrum of an aqueous dispersion of $LnFeO_3$ in the buffer solution was recorded under the same experimental conditions used for the calibration curve data and the amount of free Ln^{3+} was estimated from the curve (Fig. S5B). 2 mM aqueous suspensions of the NPs, stored at 4 ºC for a week, were incubated in 1.5 mL of 20 mM xylenol orange solution (pH 7.4) to allow free Ln^{3+} ions to form a complex with the arsenazo ligand. The resultant suspension was filtered through a 0.45 µm filter. The filtrate was then analysed at 0.5 nm on a Jasco V-560 UV/VIS spectrophotometer. Quartz cells (10 mm path length) were used. Water and a 0.076 mM $GdCl_3$ solution were used as negative and positive controls respectively.

Cell internalization and cytotoxicity of NPs: Hela cells were grown in Dulbecco's modified Eagle's medium (DMEM) supplemented with 10 % (v/v) fetal bovine serum (FBS), 10 U/mL penicillin, and 10 µg/mL streptomycin at 37 °C in fully humidified air containing 5 % CO_2. The cells were fed every 2–3 d. The cells were passaged after reaching 80 % confluency. Cells (5×10^5 cells/well) were plated in six-well plates and left to adhere overnight. Then, the cells were incubated with $EuFeO_3$, $TbFeO_3$ and $GdFeO_3$ (50 µg/mL) for 2, 4 and 6 h. After incubation, to remove non-internalized NPs, the cells were washed three times with phosphate-buffered saline (PBS), dissociated with trypsin [0.2 % (w/v) in PBS], centrifuged and counted. Afterwards, the samples were freeze-dried, and the presence of Fe, Gd and Eu, Tb in the samples was evaluated by ICP-MS (ICP/OES (ES720, Varian) equipped with a crossflow nebulizer). For this purpose, the samples were digested overnight in the presence of nitric acid [0.5 mL, 68 %, (w/v)], and hydrofluoric acid [0.5 mL, 48 % (w/v)]. Dilution of the sample was performed by addition of 1 mL of ddH_2O. The samples (n = 3) were analyzed by ICP-MS to quantify internalized elements (Fe, Eu, Tb and Gd).[94]

Cell toxicity was evaluated by the effect of NPs on ATP production. Hela cells (7 x10^3 cells/well) were seeded onto a 96-well plate and left to adhere. The cells were then incubated for 4h with NPs with different concentrations (7.8125, 15.625, 31.25, 62.5, 125, 250 µg/mL). After incubation, to remove non-internalized NPs, the cells were washed three times with phosphate-buffered saline (PBS). After 24h, ATP production was measured by a Celltiter-Glo Luminescent Cell Viability Assay (Promega) on a Synergy H1 Multi-Mode Reader (BioTek Instruments).

Supporting Information (see footnote on the first page of this article): **FigureS1**. Size distributions of the a) $EuFeO_3$and b) $TbFeO_3$ NPs estimated on a minimum of 100 measurements.

Figure S2. Zeta potential titrations as a function of pH for $GdFeO_3$ (●), $EuFeO_3$ (●) and $TbFeO_3$ (●) NPs in aqueous solution.

Figure S3. Plots of relaxation rates R_1 ($1/T_1$) as a function of $LnFeO_3$ concentration 20 MHz at a) 298 K and b) 310 K the corresponding linear regressions. I- Gd^{3+}; II- Eu^{3+} and III- Tb^{3+}.**)**;

Figure S4. Plots of relaxation rates R_2 ($1/T_2$) as a function of $LnFeO_3$ concentration 20 MHz at a) 298 K and b) 310 K the corresponding linear regressions. I- Gd^{3+}; II- $Eu^{3+}$and III- Tb^{3+}.

Figure S5. A) Spectrophotometric determination of free Ln^{3+} complexed by xylenol orange. The increase in Gd^{3+} concentration causes a decrease of the band intensity at 433nm and a corresponding increase of the band a t 563nm. The spectra were recorded in acetic buffer solution at pH 5.8 in the presence of 0, 1, 6, 10, 16, 26, 30, 36, 40, 60 and 70 □M of Gd^{3+}, respectively. B) Calibration curve obtained by spectrophotometric changes of xylenol Orange absorptions in

the presence of different amounts of Ln^{3+}, and free Ln^{3+} from the respective $EuFeO_3$, $GdFeO_3$, and $TbFeO_3$ NPs.

Acknowledgements

This work was supported by the Fundação para a Ciência e Tecnologia (FCT), Portugal (grants to SLCP (SFRH / BPD / 96048 / 2013), and project PTDC/CTM/73243/2006), the CNRS, the Région Aquitaine France, FEDER, COST Action D38 "Metal-Based systems for Molecular Imaging Applications". This work was developed within the scope of the project CICECO-Aveiro Institute of Materials, POCI-01-0145-FEDER-007679 (FCT Ref. UID /CTM /50011/2013), financed by national funds through the FCT/MEC and when appropriate co-financed by FEDER under the PT2020 Partnership Agreement. JSA acknowledges FCT IF/01089/2015 grant.

Keywords: Nanocrystals / Lanthanides/ Orthoferrites/ Relaxivity / MRI contrast agents

[1] P. Caravan, J. J. Ellison, T. J. McMurry, R. B. Lauffer, *Chem. Rev. (Washington, D. C.)* **1999**, *99*, 2293-2352.
[2] A. Merbach, L. Helm, E. Toth, Editors, *The Chemistry of Contrast Agents in Medical Magnetic Resonance Imaging*, John Wiley & Sons Ltd., **2013**.
[3] C. F. G. C. Geraldes, S. Laurent, *Contrast Media Mol. Imaging* **2009**, *4*, 1-23.
[4] S. Laurent, J.-L. Bridot, L. Vander Elst, R. N. Muller, *Future Med. Chem.* **2010**, *2*, 427-449.
[5] S. Laurent, D. Forge, M. Port, A. Roch, C. Robic, L. Vander Elst, R. N. Muller, *Chem. Rev. (Washington, DC, U. S.)* **2008**, *108*, 2064-2110.
[6] S. L. C. Pinho, H. Faneca, C. F. G. C. Geraldes, M.-H. Delville, L. D. Carlos, J. Rocha, *Biomaterials* **2012**, *33*, 925-935.
[7] S. L. C. Pinho, H. Faneca, C. F. G. C. Geraldes, J. Rocha, L. D. Carlos, M.-H. Delville, *Eur. J. Inorg. Chem.* **2012**, *2012*, 2828-2837.
[8] S. L. C. Pinho, S. Laurent, J. Rocha, A. Roch, M.-H. Delville, S. Mornet, L. D. Carlos, L. Vander Elst, R. N. Muller, C. F. G. C. Geraldes, *J. Phys. Chem. C* **2012**, *116*, 2285-2291.
[9] S. L. C. Pinho, G. A. Pereira, P. Voisin, J. Kassem, V. Bouchaud, L. Etienne, J. A. Peters, L. D. Carlos, S. Mornet, C. F. G. C. Geraldes, J. Rocha, M.-H. Delville, *ACS Nano* **2010**, *4*, 5339-5349.
[10] R. Xing, G. Liu, J. Zhu, Y. Hou, X. Chen, *Pharmaceutical Research* **2014**, *31*, 1377-1389.
[11] S. Roux, O. Tillement, C. Billotey, J.-L. Coll, G. Le Duc, C. A. Marquette, P. Perriat, *Int. J. Nanotechnol.* **2010**, *7*, 781-801.
[12] J.-L. Bridot, A.-C. Faure, S. Laurent, C. Riviere, C. Billotey, B. Hiba, M. Janier, V. Josserand, J.-L. Coll, L. Vander Elst, R. Muller, S. Roux, P. Perriat, O. Tillement, *J. Am. Chem. Soc.* **2007**, *129*, 5076-5084.
[13] F. Lux, S. Roux, P. Perriat, O. Tillement, *Curr. Inorg. Chem.* **2011**, *1*, 117-129.
[14] M.-A. Fortin, R. M. Petoral, Jr., F. Soederlind, A. Klasson, M. Engstroem, T. Veres, P.-O. Kaell, K. Uvdal, *Nanotechnology* **2007**, *18*, 395501/395501-395501/395509.
[15] J. Cheon, J.-H. Lee, *Accounts of Chemical Research* **2008**, *41*, 1630-1640.
[16] J. R. McCarthy, R. Weissleder, *Advanced Drug Delivery Reviews* **2008**, *60*, 1241-1251.
[17] J. Gao, H. Gu, B. Xu, *Accounts of Chemical Research* **2009**, *42*, 1097-1107.
[18] Q. Le Trequesser, G. Devès, G. Saez, L. Daudin, P. Barberet, C. Michelet, M.-H. Delville, H. Seznec, *Analytical Chemistry* **2014**, *86*, 7311-7319.
[19] F. Li, D. Zhi, Y. Luo, J. Zhang, X. Nan, Y. Zhang, W. Zhou, B. Qiu, L. Wen, G. Liang, *Nanoscale* **2016**, *8*, 12826-12833.
[20] M. Yang, L. Gao, K. Liu, C. Luo, Y. Wang, L. Yu, H. Peng, W. Zhang, *Talanta* **2015**, *131*, 661-665.
[21] N. A. Keasberry, M. Banobre-Lopez, C. Wood, G. J. Stasiuk, J. Gallo, N. J. Long, *Nanoscale* **2015**, *7*, 16119-16128.
[22] J.-s. Choi, J.-H. Lee, T.-H. Shin, H.-T. Song, E. Y. Kim, J. Cheon, *Journal of the American Chemical Society* **2010**, *132*, 11015-11017.
[23] Z. Zhou, D. Huang, J. Bao, Q. Chen, G. Liu, Z. Chen, X. Chen, J. Gao, *Advanced Materials* **2012**, *24*, 6223-6228.
[24] M. A. Peña, J. L. G. Fierro, *Chemical Reviews* **2001**, *101*, 1981-2018.
[25] V. V. Kharton, A. A. Yaremchenko, A. V. Kovalevsky, A. P. Viskup, E. N. Naumovich, P. F. Kerko, *Journal of Membrane Science* **1999**, *163*, 307-317.
[26] D. S. Schmool, N. Keller, M. Guyot, R. Krishnan, M. Tessier, *J. Magn. Magn. Mater.* **1999**, *195*, 291-298.
[27] E. Traversa, S. Matsushima, G. Okada, Y. Sadaoka, Y. Sakai, K. Watanabe, *Sensors and Actuators B: Chemical* **1995**, *25*, 661-664.
[28] N. Keller, J. Mistrik, S. Visnovsky, D. S. Schmool, Y. Dumont, P. Renaudin, M. Guyot, R. Krishnan, *Eur. Phys. J. B* **2001**, *21*, 67-73.
[29] N. Kojima, K. Tsushima, *Low Temp. Phys.* **2002**, *28*, 480-490.
[30] S. V. Chavan, A. K. Tyagi, *J. Mater. Res.* **2005**, *20*, 2654-2659.
[31] M. Sivakumar, A. Gedanken, D. Bhattacharya, I. Brukental, Y. Yeshurun, W. Zhong, Y. W. Du, I. Felner, I. Nowik, *Chem. Mater.* **2004**, *16*, 3623-3632.
[32] S. Mathur, H. Shen, N. Lecerf, A. Kjekshus, H. Fjellvåg, G. F. Goya, *Advanced Materials* **2002**, *14*, 1405-1409.
[33] J.-H. Lee, Y. K. Jeong, J. H. Park, M.-A. Oak, H. M. Jang, J. Y. Son, J. F. Scott, *Physical Review Letters* **2011**, *107*, 117201.
[34] Y. K. Jeong, J.-H. Lee, S.-J. Ahn, S.-W. Song, H. M. Jang, H. Choi, J. F. Scott, *Journal of the American Chemical Society* **2012**, *134*, 1450-1453.
[35] S. Cao, L. Chen, W. Zhao, K. Xu, G. Wang, Y. Yang, B. Kang, H. Zhao, P. Chen, A. Stroppa, R.-K. Zheng, J. Zhang, W. Ren, J. Íñiguez, L. Bellaiche, *Scientific Reports* **2016**, *6*, 37529.
[36] V. M. Goldschmidt, T. Barth, G. Lunde, W. Zachariasen, *Skrifter Norske Videnskaps-Akad. Oslo, Mat.-Nat. Kl.* **1926**, *No. 2*, 117 pp.
[37] S. Geller, *Acta Crystallogr.* **1956**, *9*, 885-889.
[38] S. Geller, E. A. Wood, *Acta Crystallogr.* **1956**, *9*, 563-568.
[39] Y. Sadaoka, K. Watanabe, Y. Sakai, M. Sakamoto, *J. Alloys Compd.* **1995**, *224*, 194-198.
[40] N. Kondo, H. Itoh, M. Kurihara, M. Sakamoto, H. Aono, Y. Sadaoka, *Journal of Alloys and Compounds* **2006**, *408-412*, 1026-1029.
[41] C. Vázquez-Vázquez, P. Kögerler, M. A. López-Quintela, R. D. Sánchez, J. Rivas, *Journal of Materials Research* **1998**, *13*, 451-456.
[42] X. Niu, W. Du, W. Du, *Sensors and Actuators B: Chemical* **2004**, *99*, 399-404.
[43] F. Soederlind, M. A. Fortin, R. M. Petoral, Jr., A. Klasson, T. Veres, M. Engstroem, K. Uvdal, P.-O. Kaell, *Nanotechnology* **2008**, *19*, 085608/085601-085608/085608.
[44] X. Qi, J. Zhou, Z. Yue, Z. Gui, L. Li, *Ceramics International* **2003**, *29*, 347-349.
[45] S. Farhadi, Z. Momeni, M. Taherimehr, *Journal of Alloys and Compounds* **2009**, *471*, L5-L8.
[46] S. S. Manoharan, K. C. Patil, *Journal of Solid State Chemistry* **1993**, *102*, 267-276.
[47] H.-B. Park, H.-J. Kweon, Y.-S. Hong, S.-J. Kim, K. Kim, *Journal of Materials Science* **1997**, *32*, 57-65.
[48] Z. Yue, J. Zhou, L. Li, H. Zhang, Z. Gui, *Journal of Magnetism and Magnetic Materials* **2000**, *208*, 55-60.
[49] K. D. Martinson, I. S. Kondrashkova, V. I. Popkov, *Russian Journal Of Applied Chemistry* **2017**, *90*, 1214-1218.
[50] H. Xu, X. Hu, L. Zhang, *Crystal Growth & Design* **2008**, *8*, 2061-2065.
[51] S. Hosokawa, H.-J. Jeon, S. Iwamoto, M. Inoue, *Journal of the American Ceramic Society* **2009**, *92*, 2847-2853.
[52] W. Zheng, R. Liu, D. Peng, G. Meng, *Materials Letters* **2000**, *43*, 19-22.
[53] M. Marezio, J. P. Remeika, P. D. Dernier, *Acta Crystallographica Section B* **1970**, *26*, 2008-2022.
[54] Z. Zhou, L. Guo, H. Yang, Q. Liu, F. Ye, *Journal of Alloys and Compounds* **2014**, *583*, 21-31.
[55] R. D. Shannon, *Acta Crystallogr., Sect. A* **1976**, *A32*, 751-767.
[56] M. Ristic, S. Popović, S. Musić, *J Mater Sci Lett* **1990**, *9*, 872-875.
[57] X. Liu, M. Jin, M. Liu, *Hyperfine Interact* **1992**, *68*, 241-244.
[58] X. Liu, M. Jin, C. Zhang, *Journal of Applied Physics* **1992**, *71*, 5111-5114.
[59] R. Zboril, M. Mashlan, D. Petridis, *Chemistry of Materials* **2002**, *14*, 969-982.
[60] S. M. Aliev, I. K. Kamilov, M. M. Guseinov, S. O. Shakhshaev, A. K. Abduev, *Russ. Phys. J.* **2004**, *47*, 189-193.
[61] S. B. Kim, S. J. Moon, S. J. Kim, C. S. Kim, *Journal of Magnetism and Magnetic Materials* **2007**, *310*, e592-e594.
[62] L. J. Downie, R. J. Goff, W. Kockelmann, S. D. Forder, J. E. Parker, F. D. Morrison, P. Lightfoot, *Journal of Solid State Chemistry* **2012**, *190*, 52-60.
[63] M. Florea, M. Alifanti, V. Kuncser, V. I. Parvulescu, *Catalysis Today* **2013**, *208*, 56-59.
[64] H. Yang, J. X. Zhang, G. J. Lin, T. Xian, J. L. Jiang, *Adv. Powder Technol.* **2013**, *24*, 242-245.

[65] S. M. Aliev, I. K. Kamilov, M. S. Aliev, Z. G. Ibaev, *Phys. Solid State* **2014**, *56*, 1114-1117.
[66] M. Florea, M. Alifanti, V. Kuncser, D. Macovei, N. Apostol, P. Granger, V. I. Parvulescu, *J Catal* **2014**, *316*, 130-140.
[67] O. Opuchovic, A. Kareiva, K. Mazeika, D. Baltrunas, *J. Magn. Magn. Mater.* **2017**, *422*, 425-433.
[68] M. Eibschütz, S. Shtrikman, D. Treves, *Physical Review* **1967**, *156*, 562-577.
[69] D. Treves, *Journal of Applied Physics* **1965**, *36*, 1033-1039.
[70] O. Nikolov, I. Hall, S. N. Barilo, A. A. Mukhin, *J. Magn. Magn. Mater.* **1996**, *152*, 75-85.
[71] E. F. Bertaut, J. Chappert, J. Mareschal, J. P. Rebouillat, J. Sivardière, *Solid State Communications* **1967**, *5*, 293-298.
[72] J. Mareschal, J. Sivardiere, G. F. De Vries, E. F. Bertaut, *J. Appl. Phys.* **1968**, *39*, 1364-1366.
[73] A. Apostolov, J. Sivardiere, *C. R. Acad. Sci., Paris, Ser. A B* **1968**, *267B*, 1315-1318.
[74] R. M. Bozorth, H. J. Williams, D. E. Walsh, *Phys. Rev.* **1956**, *103*, 572-578.
[75] R. M. Bozorth, *Phys. Rev. Lett.* **1958**, *1*, 362-363.
[76] R. M. Bozorth, V. Kramer, J. P. Remeika, *Phys. Rev. Lett.* **1958**, *1*, 3-4.
[77] M. Robbins, R. D. Pierce, R. Wolfe, *J. Phys. Chem. Solids* **1971**, *32*, 1789-1796.
[78] M. Norek, J. A. Peters, *Prog. Nucl. Magn. Reson. Spectrosc.* **2011**, *59*, 64-82.
[79] N. Luo, X. Tian, J. Xiao, W. Hu, C. Yang, L. Li, D. Chen, *J. Appl. Phys. (Melville, NY, U. S.)* **2013**, *113*, 164306/164301-164306/164306.
[80] Y. Gossuin, A. Hocq, Q. L. Vuong, S. Disch, R. P. Hermann, P. Gillis, *Nanotechnology* **2008**, *19*, 475102/475101-475102/475108.
[81] M. Norek, G. A. Pereira, C. F. G. C. Geraldes, A. Denkova, W. Zhou, J. A. Peters, *J. Phys. Chem. C* **2007**, *111*, 10240-10246.
[82] G. Goglio, G. Kaur, S. L. C. Pinho, N. Penin, A. Blandino, C. F. G. C. Geraldes, A. Garcia, M.-H. Delville, *Eur. J. Inorg. Chem.* **2015**, 1243-1253.
[83] L. Zhou, Z. Gu, X. Liu, W. Yin, G. Tian, L. Yan, S. Jin, W. Ren, G. Xing, W. Li, X. Chang, Z. Hu, Y. Zhao, *Journal of Materials Chemistry* **2012**, *22*, 966-974.
[84] J. Y. Park, K. Kattel, W. Xu, H. G. Kim, E. J. Lee, G. H. Lee, J. J. Lee, Y. Chang, T. J. Kim, *J. Korean Phys. Soc.* **2011**, *59*, 2376-2380.
[85] Z. Hu, M. Ahren, L. Selegard, C. Skoglund, F. Soederlind, M. Engstroem, X. Zhang, K. Uvdal, *Chem. - Eur. J.* **2013**, *19*, 12658-12667.
[86] N. Luo, X. Tian, C. Yang, J. Xiao, W. Hu, D. Chen, L. Li, *Physical Chemistry Chemical Physics* **2013**, *15*, 12235-12240.
[87] D. Vandormael, F. Grandjean, D. Hautot, G. J. Long, *J. Phys.: Condens. Matter* **2001**, *13*, 1759-1772.
[88] J. H. Jensen, R. Chandra, *Magnetic Resonance in Medicine* **2000**, *44*, 144-156.
[89] P. Gillis, F. Moiny, R. A. Brooks, *Magnetic Resonance in Medicine* **2002**, *47*, 257-263.
[90] A. Roch, Y. Gossuin, R. N. Muller, P. Gillis, *Journal of Magnetism and Magnetic Materials* **2005**, *293*, 532-539.
[91] A. Barge, G. Cravotto, E. Gianolio, F. Fedeli, *Contrast Media & Molecular Imaging* **2006**, *1*, 184-188.
[92] S. P. M. Crouch, R. Kozlowski, K. J. Slater, J. Fletcher, *Journal of Immunological Methods* **1993**, *160*, 81-88.
[93] M. A. Malvindi, V. De Matteis, A. Galeone, V. Brunetti, G. C. Anyfantis, A. Athanassiou, R. Cingolani, P. P. Pompa, *PLoS One* **2014**, *9*, e85835/85831-e85835/85811, 85811 pp.
[94] A. M. Alkilany, P. K. Nagaria, C. R. Hexel, T. J. Shaw, C. J. Murphy, M. D. Wyatt, *Small* **2009**, *5*, 701-708.

Entry for the Table of Contents (Please choose one layout)

Layout 1:

FULL PAPER

Synthesis and characterization of rare earth orthoferrite $LnFeO_3$ NPs for bioimaging

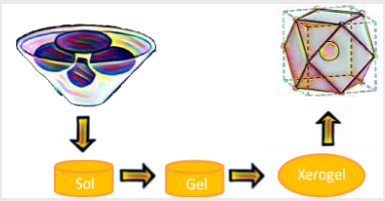

Key Topic* rare earth orthoferrite $LnFeO_3$ nanoparticles as MRI CA.

Sonia L.C. Pinho, João S. Amaral, Alain Wattiaux, Mathieu Duttine, Marie-Hélène Delville, and Carlos F.G.C. Geraldes**

Page No. – Page No.

*one or two words that highlight the emphasis of the paper or the field of the study